

# Formation and Optical Properties of ZnO:ZnFe<sub>2</sub>O<sub>4</sub> Superlattice Microwires

Yun Li<sup>1,†</sup>, Guozhang Dai<sup>1,2,†</sup>, Chunjiao Zhou<sup>1</sup>, Qinglin Zhang<sup>1</sup>, Qiang Wan<sup>1</sup>, Limin Fu<sup>3</sup>, Jianping Zhang<sup>3</sup>, Ruibin Liu<sup>2</sup>, Chuanbao Cao<sup>2</sup>, Anlian Pan<sup>2</sup>, Yunhong Zhang<sup>2</sup>, and Bingsuo Zou<sup>1,2</sup> (✉)

<sup>1</sup> State Key Laboratory of Chemo/biosensing and Chemometrics (CBSC), Hunan University, Changsha 410082, China

<sup>2</sup> School of Materials Science and Engineering (MSE), Beijing Institute of Technology, Beijing 100081, China

<sup>3</sup> Chemistry Department, Renmin University of China, Beijing 100872, China

Received: 28 January 2010 / Revised: 5 March 2010 / Accepted: 5 March 2010

© The Author(s) 2010. This article is published with open access at Springerlink.com

## ABSTRACT

Pure ZnO hexagonal microwires and Fe(III)-doped ZnO microwires (MWs) with a novel rectangular cross section were synthesized in a confined chamber by a convenient one-step thermal evaporation method. An oriented attachment mechanism is consistent with a vapor–solid growth process. Photoluminescence (PL) and Raman spectroscopy of the Fe(III)-doped ZnO MWs and *in situ* spectral mappings indicate a quasi-periodic distribution of Fe(III) along a one-dimensional (1-D) superlattice ZnO:ZnFe<sub>2</sub>O<sub>4</sub> wire, while PL mapping shows the presence of optical multicavities and related multimodes. The PL spectra at room temperature show weak near-edge doublets (376 nm and 383 nm) and a broad band (450–650 nm) composed of strong discrete lines, due to a 1-D photonic crystal structure. Such a 1-D coupled optical cavity material may find many applications in future photonic and spintronic devices.

## KEYWORDS

ZnO, superlattice microwire, micro-photoluminescence, micro-Raman spectroscopy

## 1. Introduction

Semiconductor nanowires (NWs) have attracted more and more attention in recent years for their extensive applications in nanoscale photonic lasers [1–7]. For a long time, attention in this area has focused on ZnO NWs due to their excellent material properties such as a wide band gap (3.37 eV) and large exciton binding energy (60 meV) at room temperature. In the initial stages, the predominant applications of ZnO were in optics, optoelectronic devices, sensors, photocatalysis, and actuators [8–12]. Its nanostructures have been

recently reported to be of potential use in different kinds of nanodevices such as nanolasers, transistors, spintronic devices, gas sensors, waveguides, and field emitters [1, 13–16]. Incorporation of small amounts of transition metal ions into ZnO NWs has been shown to be a good method to control their optical properties [17]. Transition metal (TM) doped-ZnO NWs have been widely investigated because of their ferromagnetic and magnetic transport properties as diluted magnetic semiconductors (DMSs). More and more work on the magnetic properties of Cu- [18], Co- [19], Mn- [20], and Ni- [21] doped ZnO nanostructures has been

<sup>†</sup> These authors contributed equally to this work.  
Address correspondence to zoubs@bit.edu.cn

reported in recent years. Although the vast majority of studies of DMS materials have been carried out on bulk or thin film samples [22, 23], a few reports have been published recently on TM-doped ZnO nanorods and nanobelts [17, 24]. Although a few reports covering the optical properties of Fe(III)-doped ZnO nanostructures have appeared [25–27], the morphologies of the materials involved seldom showed the appearance of perfect NWs.

The development of photonic crystals (PCs), which are materials with a periodically modulated refractive index, has opened up a new field for photon confinement and modulation. Over the past several years, many artificial two- and three-dimensional PCs have been developed for this reason, and can be used in new photonic devices like light waveguides, sensors, filters, and light emitters. However, one-dimensional (1-D) PCs have attracted less attention in spite of their simple energy band diagram and unique transport properties. In fact, artificial PCs produced by various etching techniques always contain many imperfections at their boundaries, so it is challenging to find an effective way to produce 1-D PC systems. Our approach to this problem is to try to grow 1-D nano- to micrometer sized wires with a PC structure based on multiple components with varying refractive indices.

Applications in optoelectronics of single ZnO NWs serving as an optical cavity have been previously reported [1, 2, 28–31]. Admirable results have been obtained due to the well-defined end facets of their NW microcavities and the associated unique optical confinement and microcavity effects [1, 31, 32]. However, a 1-D PC microwire (MW) with microcavities has not been studied so far.

In the present work, we present a very simple one-step vapor transport and condensation method to grow ZnO:ZnFe<sub>2</sub>O<sub>4</sub> 1-D PCs with rectangular cross section. A detailed analysis has been carried out of the mechanism of formation of the rectangular cross section of these MWs. Room-temperature Raman spectroscopy and photoluminescence (PL) spectroscopy with their respective *in situ* mapping profiles have been obtained with a scanning near-field optical microscope (SNOM). Many new optical cavity modes in the visible range occur as a result of the incorporation of Fe(III) in the MWs. Furthermore, the cavity-mode

emission peaks show a good correlation with the Fabry–Pérot (F–P) modes of the MW cavity.

## 2. Experimental

The ZnO:ZnFe<sub>2</sub>O<sub>4</sub> MW PCs were prepared using a convenient physical thermal evaporation method. All of the reagents were analytical grade and used without any further purification. Typically, ZnO powder, carbon powder, and Fe<sub>2</sub>O<sub>3</sub> powder with the mass ratio of 1:2:0.2 were mixed thoroughly and loaded on an alumina boat. The boat was then positioned at the center of a quartz tube sealed at one end (diameter 2 cm, length 60 cm). The other end of the quartz tube was open to the atmosphere. Another alumina boat loaded with several pieces of silicon wafer was placed downstream at the open end of the quartz tube (about 5 cm away from the source material) to collect the products. Before the silicon substrate was loaded into the furnace, it was ultrasonically cleaned in ethanol for 5 min, rinsed with distilled water and then coated by an Au nanofilm of 2 nm in thickness. The quartz tube was pushed into a horizontal tube furnace. The furnace was heated to 1000 °C and maintained at this temperature for 30 min before being cooled down to room temperature. During the whole process, an argon flow of 5 standard cubic centimeters per minute (sccm) was introduced as the protecting gas. White-colored products formed on the silicon wafer and on the inner walls of the quartz tube in the region with temperatures ranging from 500 to 900 °C. The whole growth process is very sensitive to the conditions and the growth time plays a significant role in the controlling the formation and particle size of the products.

The morphologies and microstructures of the products were investigated using a Hitachi JEOL JSM-6700F field-emission scanning electron microscope (FESEM) equipped with an energy-dispersive X-ray spectroscopy (EDS) attachment and a JEM 3010 high-resolution transmission electron microscope (HRTEM) working at 200 kV. The samples were characterized by powder X-ray diffraction (XRD), using a Siemens D-5000 X-ray diffractometer equipped with graphite-monochromated Cu K $\alpha$  radiation ( $\lambda = 1.541874 \text{ \AA}$ ), with an operating voltage and current



maintained at 40 kV and 40 mA, respectively. The room-temperature PL spectra and Raman spectra were obtained using a commercial near-field scanning optical microscope (NSOM) (WITec alpha300) with a He–Cd laser (10 mW, wavelength of 325 nm, Hitachi) and an Ar<sup>+</sup> laser (20 mW, wavelength of 488 nm), respectively.

### 3. Results and discussion

The XRD pattern of the as-prepared Fe(III)-doped product is shown in Fig. 1(b). Comparison with the XRD pattern for a pure ZnO NW (Fig. 1(a)) shows that most of the observed peaks can be indexed to a hexagonal wurtzite phase of ZnO with lattice constants of  $a = 3.25 \text{ \AA}$  and  $c = 5.21 \text{ \AA}$ ; these values are in agreement with the reported values (Joint Committee on Powder Diffraction Standards (JCPDS) Card No. 36-1451). In addition to peaks from hexagonal ZnO, additional peaks marked \* in Fig. 1(b) can be attributed to a spinel ZnFe<sub>2</sub>O<sub>4</sub> phase, based on the standard JCPDS Card No. 22-1012. These diffraction peaks are shifted to higher angles as compared with the corresponding peaks for pure ZnO NWs, suggesting that the unit cell contracts to accommodate the Fe(III) ions. Such a change is indeed to be expected if Fe(III) ions replace Zn(II) ions in the lattice, since the ionic radius of Fe<sup>3+</sup> (0.064 nm) is smaller than that of Zn<sup>2+</sup> (0.074 nm) ions [33]. XRD therefore confirms that Fe(III)

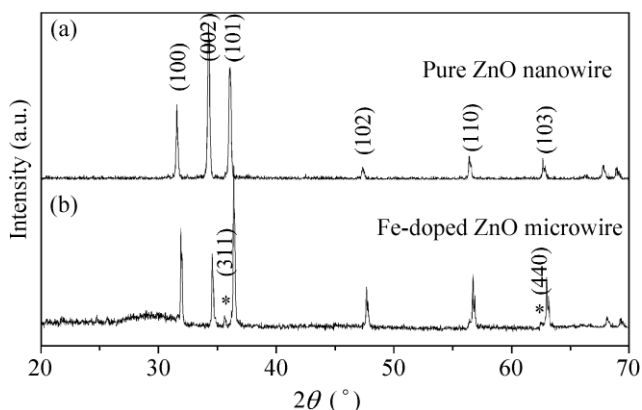


**Figure 1** XRD patterns of (a) pure ZnO nanowires and (b) as-prepared Fe-doped ZnO microwires. The peaks indexed in (a) correspond to those of a wurtzite ZnO structure with lattice constants  $a = 3.25 \text{ \AA}$  and  $c = 5.21 \text{ \AA}$ , consistent with JCPD Card No. 36-1451. Peaks marked \* in (b) are characteristic of a cubic ZnFe<sub>2</sub>O<sub>4</sub> phase (JCPDS Card No. 22-1012)

ions have been incorporated in the ZnO MWs.

Figure 2 shows typical SEM images of the as-prepared Fe(III)-doped ZnO MWs at different magnifications. In Fig. 2(a), the MWs are seen to lie flat with an average length of more than 200  $\mu\text{m}$  and a diameter ranging from about 500 nm to 2  $\mu\text{m}$ . In the high-magnification SEM image in Fig. 2(b), the rectangular or nearly square cross section and flat end faces of the MWs can be clearly identified. The well-faceted nature of these MWs is important in ensuring that they can work as an effective optical cavity. TEM (not shown, since a high-resolution TEM image could not be obtained) indicated that the MWs grow along the  $c$  axis, corresponding to the (0001) direction of ZnO. EDS performed on individual MWs confirmed the presence of Fe in each ZnO MW. The inset of Fig. 2(b) shows the EDS of a single MW, which contains about 0.5% atomic concentration of Fe in addition to the Zn and O elements (the carbon peak originates from the residual carbon powder in the reactants), which is consistent with the XRD pattern. The EDS analyses of different single MWs indicate that the atomic concentration of Fe varies from 0.1% to 2%. It should be mentioned that the MWs with Fe(III) content of more than about 1% show a dark color in optical microscopy and are poor light emitters. Conduction measurements indicated that the doped wires have semimetal conductivity at low temperature, in contrast to ZnO NWs.

How do the rectangular cross-sectional MWs form? There have been previous reports of ZnO and ZnS wurtzite NWs with rectangular and square cross sections [34, 35]. The vapor–liquid–solid mechanism [34] is not applicable here because we do not see any particles at the tip of the MWs or NWs. A vapor–solid (VS) mechanism can account for the growth of formations like a ribbon, and the details of the growth process should depend on the growth time. We found that the appearance of the MWs did indeed vary with the growth time. Figure 3(a) shows the SEM images of a sample with a hexagonal cross section formed when the growth time was about 10 min, with a HRTEM image shown in the inset.

For longer growth time, the growth of the ZnO wire depends on the relative amounts of Zn and Fe

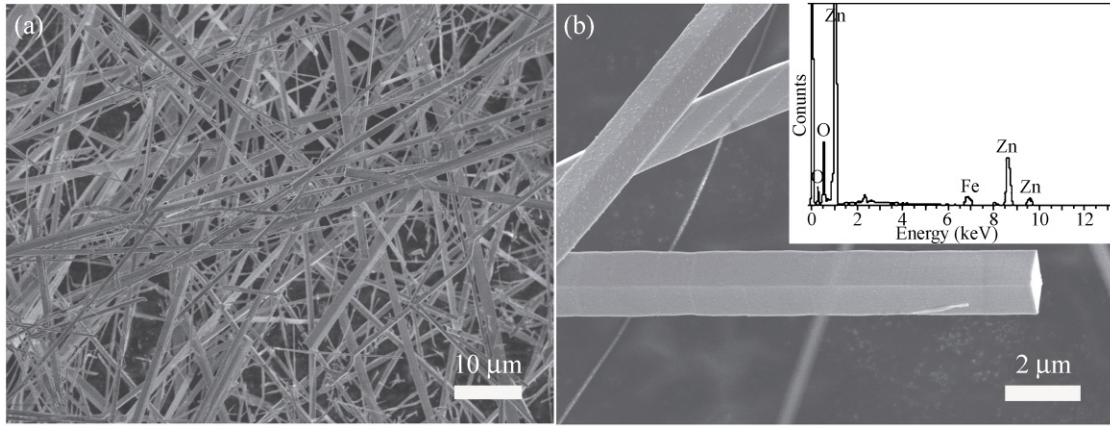


**Figure 2** Typical SEM images of as-prepared Fe-doped ZnO MWs: (a) low-resolution SEM image; (b) higher-resolution image of a single MW with flat end faces, with rectangular or nearly square cross sections; the inset is the EDS spectrum of the single MW with a Fe content of 0.5%

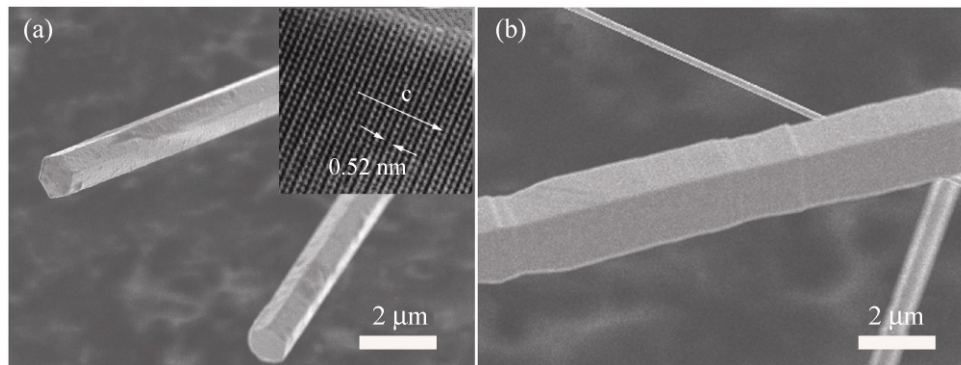
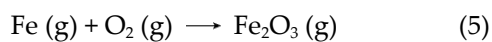
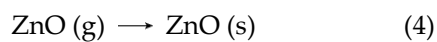
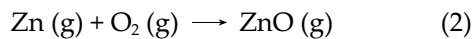
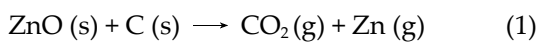


**Figure 3** SEM images of samples prepared with different reaction time of (a) ~10 min (the inset shows the HRTEM image) and (b) 20–30 min

since they have different growth habits. The following reactions are involved in the growth process:



In the initial stages ZnO (g) will predominate and much less Fe<sub>2</sub>O<sub>3</sub> (g) will be produced by virtue of their different heats of formation ZnO (348.3 kJ/mol) and

Fe<sub>2</sub>O<sub>3</sub> (824.2 kJ/mol). The heat of formation of ZnO refers to the reaction Zn (s) + O<sub>2</sub> (g) → ZnO (s) and is exothermic (−348.3 kJ/mol). The heat of formation of Fe (s) + O<sub>2</sub> (g) → Fe<sub>2</sub>O<sub>3</sub> (s) is −824.2 kJ/mol. The reactions shown in reactions (1) and (2) predominate in the earlier stages, leading to the formation of hexagonal-ZnO wires via reaction (4), as illustrated in Figs. 4(a) and 4(b). There are two reasons for the preferential growth of ZnO wires: (1) the amount of the ZnO precursor is in large excess over that of Fe<sub>2</sub>O<sub>3</sub>; (2) ZnO and Fe<sub>2</sub>O<sub>3</sub> have different activation energies, with Fe<sub>2</sub>O<sub>3</sub> needing more energy to become vaporized and the minor amount of Fe (g) present has a negligible effect on ZnO nanostructure formation.

When the reaction time reaches about 20 min, most of the ZnO (g) has been consumed and reactions (3) and (5) increase in importance so that the overall



concentration of gaseous ZnO and Fe<sub>2</sub>O<sub>3</sub> decreases. VS growth, similar to that observed during oriented attachment in solution, dominates at this time and ZnFe<sub>2</sub>O<sub>4</sub> will form and participate in the VS growth. Both ZnO and ZnFe<sub>2</sub>O<sub>4</sub> deposit on the surface of the hexagonal ZnO wires via reactions (4) and (6), respectively, forming an irregular structure with ZnFe<sub>2</sub>O<sub>4</sub> attached/wrapped around ZnO (as shown in Fig. 3(b)), due to the difference in the growth rates of Fe<sub>2</sub>O<sub>3</sub> and ZnO. The processes are illustrated by the cartoons in Figs. 4(b) and 4(c). Since ZnFe<sub>2</sub>O<sub>4</sub> is a cubic crystal, it tends to form a wire with rectangular cross section. Thus, subsequent further growth of ZnFe<sub>2</sub>O<sub>4</sub> converts the hexagonal NWs into thicker MWs with a rectangular cross section, as in shown in Fig. 3(b). An HRTEM image cannot be obtained of such a wire. This transformation is similar to the oriented attachment mechanism in solution shown in Ref. [35]. On further prolonging the growth time to about 30 min, the reactants all become completely consumed, and the ZnFe<sub>2</sub>O<sub>4</sub> (or Fe<sup>3+</sup>) on the surface of the ZnO can migrate to some extent into the core of the ZnO wire, forming a periodic ZnFe<sub>2</sub>O<sub>4</sub>:ZnO MW. This process is similar to the partial cation diffusion mechanism which has been reported in the spontaneous formation of superlattice nanorods [36]. The distribution of alternate ZnFe<sub>2</sub>O<sub>4</sub> segments in the final ZnO wire should lead to the minimum stress in the whole wire, and will promote the stability and result in a striped pattern (Fig. 4(d)). In further experiments, we found lower amounts of Fe<sub>2</sub>O<sub>3</sub> (mass ratio of Fe<sub>2</sub>O<sub>3</sub>:ZnO < 3%) and longer (>40 min) reaction time favor the formation of metallic MWs with a higher Fe population, which is consistent with the partial cation diffusion mechanism proposed in this work. However, the product with higher Fe population is out of the realm of our discussion on its optical behavior. This experiment indicates that the composition is not positive on the precursor ratio.

The Raman spectrum of a solid provides abundant structural information, and Raman spectroscopy is a powerful tool for fast and non-destructive detection of the vibrational modes of a dopant, particularly useful when impurity-induced modes can be traced back to individual constituents. According to the XRD pattern, the MWs have a wurtzite structure, with two formula units per primitive cell. The normal vibrational modes

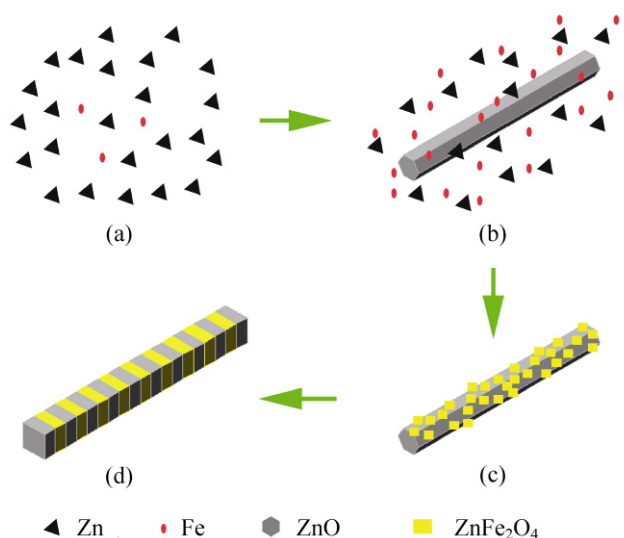


**Figure 4** Schematic illustration of the growth process of periodic ZnO:ZnFe<sub>2</sub>O<sub>4</sub> MWs

for wurtzite ZnO are  $A_1 + 2E_2 + 2B_2 + E_1$ , of which  $A_1$  and  $E_1$  are both Raman and infrared active,  $E_2$  is Raman active only, and  $B_1$  is both Raman and infrared inactive according to the selection rules for phonon resonance modes [37]. The  $A_1$  and  $E_1$  modes are polar with transverse optical ( $A_{1T}$  and  $E_{1T}$ ) and longitudinal optical ( $LO$ ,  $A_{1L}$  and  $E_{1L}$ ) phonons, and the  $E_2$  mode consists of two modes with low and high-frequency phonons ( $E_{2L}$  and  $E_{2H}$ ) [38]. The Raman spectra of the as-prepared ZnO NW and Fe-doped MW are given in Fig. 5. The excitation laser is focused onto a  $\sim 2 \mu\text{m}$  diameter spot on the sample with a  $\times 20$  microscope objective. The sample is dispersed on a cover glass but the optical losses in the glass are negligible. A chromatic color charge-coupled device (CCD) camera is used to collect the far-field topography and optical image through an objective lens. In the Raman spectrum of an undoped ZnO NW (Fig. 5(a)), the intense peak at  $437 \text{ cm}^{-1}$  can be assigned to the normal  $E_{2H}$  mode of the ZnO crystal, which is the strongest mode in the spectrum of wurtzite. The peaks at  $98$  and  $379 \text{ cm}^{-1}$  arise from the  $E_{2L}$  and  $A_{1T}$  modes, respectively, whilst the modes at  $577$  and  $593 \text{ cm}^{-1}$  correspond to  $A_{1L}$  and  $E_{1L}$ , respectively. Besides these first-order modes, the Raman spectra also show other modes with frequencies  $329$  and  $1148 \text{ cm}^{-1}$ , which are usually observed in the spectra of wurtzite materials, and are attributed to a combination of first-order modes and an overtone, identified as  $(E_{2H} - E_{2L})$  and  $(2A_{1L})$ , respectively [37].

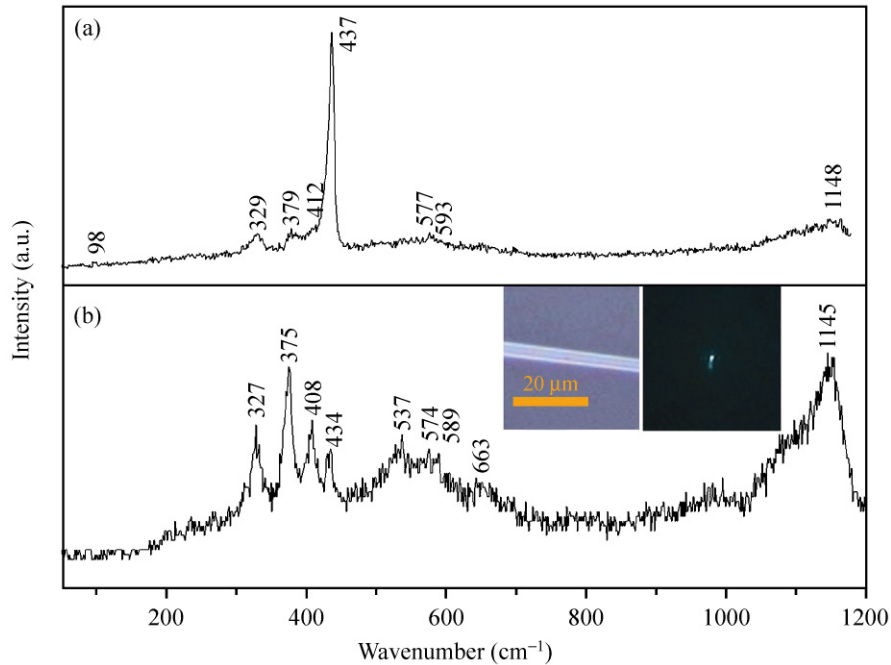


**Figure 5** Room-temperature Raman spectrum of (a) a single pure ZnO nanowire and (b) a single Fe-doped ZnO microwire (The insets in (b) show the bright (left) and dark (right) field images in the CCD camera with the laser of 488 nm focused on the microwire)

Figure 5(b) shows the Raman spectrum of doped MWs with diameter of about 2  $\mu\text{m}$  and lengths of more than 200  $\mu\text{m}$ , when the laser is focused on one MW. The Raman spectrum still shows the  $E_{2L}$ ,  $A_{1T}$ ,  $A_{1L}$ , and  $E_{1L}$  modes, which means that the crystal structure of ZnO is retained despite Fe(III) ions being incorporated into the crystal lattice through substitution of Zn(II) ions. The weak band at 408  $\text{cm}^{-1}$  can be attributed to an  $E_{1T}$  mode where the polarization is due to mixing of oriented crystallites and the breaking of selection rules for propagation in a direction other than the  $c$  crystallographic axis [38, 39]. The fact that a weak band at 408  $\text{cm}^{-1}$  corresponding to the  $E_{1T}$  mode is observed indicates that the Fe(III)-doped ZnO MWs do not grow preferentially along the  $c$ -axis. It is an evidence for the growth condition effect, which is imposed on ZnO and related  $E_{1T}$  mode scattering geometry [39]. The spectrum shows a broad and intense band ranging from 500 to 700  $\text{cm}^{-1}$ , which may be related to the presence of other carriers. The vibration centered at 537  $\text{cm}^{-1}$  can be attributed to either a local vibration mode related to the donor defects bound to Fe sites, or oxygen vacancies and Zn interstitials [40]. There are different opinions on the origin of the peak

at 663  $\text{cm}^{-1}$ : it has been attributed to both an overtone process ( $A_{1L} + E_{2L}$ ) and a dopant mode [41]. However, the former is forbidden by a strict selection rule and is expected to result in a very weak intensity band.

We now look at the dopant effect. As shown in the above section, the XRD pattern indicated the presence of  $\text{ZnFe}_2\text{O}_4$  as a minor component of the MWs. This material has a characteristic Raman band at 665  $\text{cm}^{-1}$  [26], so the peak at 663  $\text{cm}^{-1}$  in Fig. 5(b) can reasonably be assigned to  $\text{ZnFe}_2\text{O}_4$  in ZnO MWs, which further confirms these MWs are composed of two materials. It can be seen that peaks at 329, 379, 437, 577, 593, and 1148  $\text{cm}^{-1}$  shift towards lower energy (being observed at 327, 375, 434, 575, 589, and 1145  $\text{cm}^{-1}$ , respectively) after Fe(III) doping in ZnO. This shift may arise because the enhanced covalency of the Fe–O bond, may reduce the Zn–O bond strength in nearest neighbors due to the redistribution of electron density at the dopant and host atoms and this, as well as a possible carrier screening effect, can lead to the observed reduced vibrational energies [42].

For doped MWs, the 2 multiple longitudinal optic (2LO) phonon mode at 1145  $\text{cm}^{-1}$  is much stronger than that in the undoped NWs. Wang et al. have reported

that the magnitudes of the ratio of second- to first-order Raman scattering cross section increase with MW diameter, and it has been unambiguously demonstrated that electron–phonon coupling increases with nanocrystal size due to the Fröhlich interaction, which become significant for larger interaction volumes [43, 44]. As mentioned above, our MWs with an average diameter of about 1–2  $\mu\text{m}$  are much thicker than those reported previously, which may cause strong electron–phonon coupling and result in high ratios of second- to first-order Raman scattering cross section. Doping is another reason for enhanced lattice polarizability and electron–phonon coupling and can produce larger deformation potentials. Therefore, comparison of the Raman spectra of the undoped ZnO NW and the Fe(III)-doped ZnO MW suggests that there is a stronger electron–phonon coupling which dominates in the latter.

The Raman mapping technique is a way of obtaining information about the composition of an MW at the microscale level: for example, for a doped MW it can provide evidence about the distribution of the dopant along and across the MW. Figure 6 shows a simple far-field Raman mapping of a single MW. This MW is about 4  $\mu\text{m}$  in diameter and more than 2 mm in length. Figure 6(a) shows the mapping image collected from the whole range from 0 to 1371  $\text{cm}^{-1}$ . Interestingly, this mapping gives a periodic intensity profile along the MW. The length of periodic change is about 3.5–4.5  $\mu\text{m}$ . In order to explore how a single phonon mode changes in comparison with that for the undoped ZnO MWs, we mapped every peak of the first order modes in the Raman spectra. For example, when the range from 432 to 436  $\text{cm}^{-1}$  which is centered at 434  $\text{cm}^{-1}$  is scanned (Fig. 6(e)), the bright and dark parts represent the maximum and minimum intensities of this peak, respectively. Figures 6(b)–6(j) show the mapping results at 327, 375, 408, 434, 537, 575, 589, 663, and 1145  $\text{cm}^{-1}$ , respectively. Strangely, mappings of the characteristic modes for undoped ZnO at 327, 375, 408, 434, and 1145  $\text{cm}^{-1}$  show the opposite periodic profiles to that in Fig. 6(a), with bright regions corresponding to dark ones and the dark regions to the bright ones. This indicates that the mapping for all peaks represents an emission spatial profile, while single intrinsic Raman peak mapping represents the component distribution.

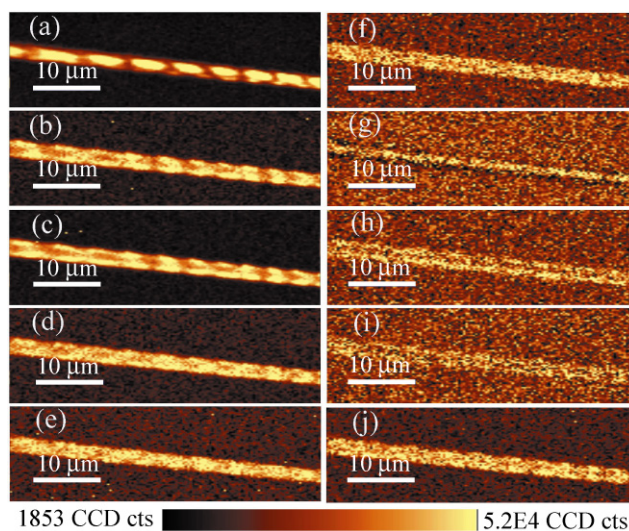


**Figure 6** Raman mapping images of all peaks for a Fe(III)-doped ZnO MW: (a) the mapping collected from the whole wavenumber range from 0 to 1370  $\text{cm}^{-1}$ ; (b)–(j) mapping results for wavenumbers of 327, 375, 408, 434, 537, 575, 589, 663, and 1145  $\text{cm}^{-1}$ , respectively

The mapping of the characteristic  $\text{ZnFe}_2\text{O}_4$  bands at 537 and 663  $\text{cm}^{-1}$  is ambiguous, which confirms that the quantity of Fe(III) dopant in the MW is low. The mappings of peaks at 575 and 589  $\text{cm}^{-1}$  are almost inverse in their locations, with the  $A_{1L}$  mode being mainly generated from internal phonons and photon scattering and the  $E_{1L}$  mode appearing on the MW surface. This indicates that after doping of Fe(III), the lattice-related electronic polarizability is enhanced, with the  $A_{1L}$  mode being polarized along the long axis and the  $E_{1L}$  mode being polarized vertical to the long axis, which differs from previously reported results [45]. From the above mapping results, we can conclude that Fe(III) doping in the MWs shows a periodic Fe distribution along the long axis of a ZnO– $\text{ZnFe}_2\text{O}_4$ –ZnO 1-D wire. This should be reflected in their photoluminescence mappings.

Therefore, room-temperature PL spectra of doped MWs were also obtained with excitation at 325 nm from a He–Cd laser; the resulting spectra and mapping are shown in Fig. 7. The excitation laser was focused onto a  $\sim 2$   $\mu\text{m}$  diameter spot on the sample with a  $\times 10$  microscope objective. The PL spectra for the MW with a sharp pyramidal end exhibit very different shapes when the laser is focused at the sharp end (Fig. 7(a)) and at the middle (Fig. 7(b)) of the MW (at the spots

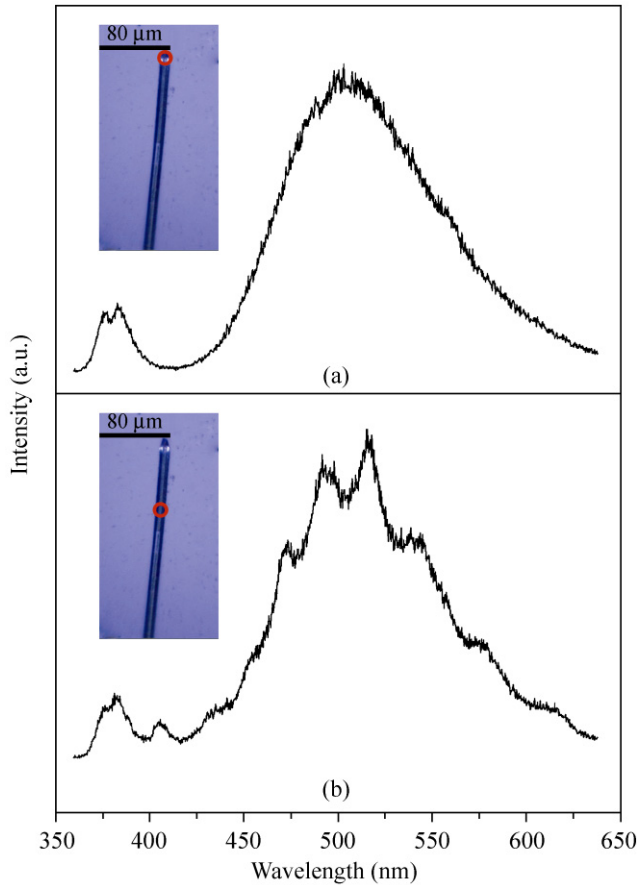


**Figure 7** Room-temperature PL spectra of a single ZnO:ZnFe<sub>2</sub>O<sub>4</sub> MW with the laser focused on (a) the sharp tapered end and (b) the body of the microwire. The insets in (a) and (b) are the bright images of the microwire (the red circles denote the spot where the laser was focused)

shown in the inset). The visible emission spectrum resulting from irradiation at the end of the MW contains a broad band without any structure, while that resulting from irradiation at the middle shows discrete emission bands.

When the laser is focused at the sharp pyramidal tip of an MW, the spectrum exhibits UV emission (Fig. 7(a)) in addition to the broad emission band in the green region centered at around 503 nm. The UV luminescence consists of two peaks, one centered at 376 nm and the other located at 383 nm. These bands are very similar to those observed in the PL spectrum of pure ZnO, which are usually attributed to the band-edge emission originating from the recombination of free excitons [20, 43]. The spacing between the two emission peaks is 60.4 meV, which may be caused by

the splitting of the free exciton [46]. Another possible origin is the multiphonon replica of free exciton emission, induced by impurities. When the laser is focused on the body of the MW, the spectrum in the UV range (Fig. 7(b)) is essentially identical to that in Fig. 7(a). The relatively strong green band centered at 503 nm may originate from the electronic transitions from the shallow donor level of oxygen vacancies and zinc interstitials to the valence band [20]. Another possibility is the d–d transition and pair excitation of Fe(III) in ZnFe<sub>2</sub>O<sub>4</sub> [47]. The presence of the discrete bands in Fig. 7(b) may indicate an optical cavity effect in the MW.

For the two PL spectra in Fig. 7, if we assume that there is a reflective facet in the MW which can form F–P optical cavities, the cavity length  $L$  can be calculated by formula [43]

$$\Delta\lambda = \lambda^2 / (2nL)$$

where  $n$  is the refractive index ( $n = 2.0$  for ZnO),  $\lambda$  is the resonant wavelength, and  $\Delta\lambda$  is the mode spacing. The calculated cavity length is about 3.4–4.5  $\mu\text{m}$ , which is much shorter than the measured length of the ZnO MWs, but very close to the length of the periodic spatial distance in the Raman peak mapping. Thus, it can be concluded that the photon oscillation does not occur between the two end facets of the wire, but rather within the inner periodic microstructure.

Figure 8(a) shows the PL spectrum of the same ZnO MW observed when recording the Raman spectrum with irradiation at 488 nm. The frequency to time Fourier transform of its visible range indicates the lifetime profile of the optical cavity mode in the spectrum (Fig. 8(b)). The real lifetime measurement for the 595 nm peak in Fig. 8(c) indicates a biexponential relaxation, which may agree with the above profile, but does not fit well to the numerical simulation (Fig. 8(b)). This difference can be explained by the fact that Fig. 8(b) is obtained from a single MW, but Fig. 8(c) comes from an array of many MWs, and the interactions between the MWs lengthen the longer component of the emission lifetime. The ultraviolet emission shows an exponential relaxation with a lifetime of 2.06 ns (not shown here). The short lifetime dominates the NW emission within the laser pulse scale, indicating an optical cavity effect with



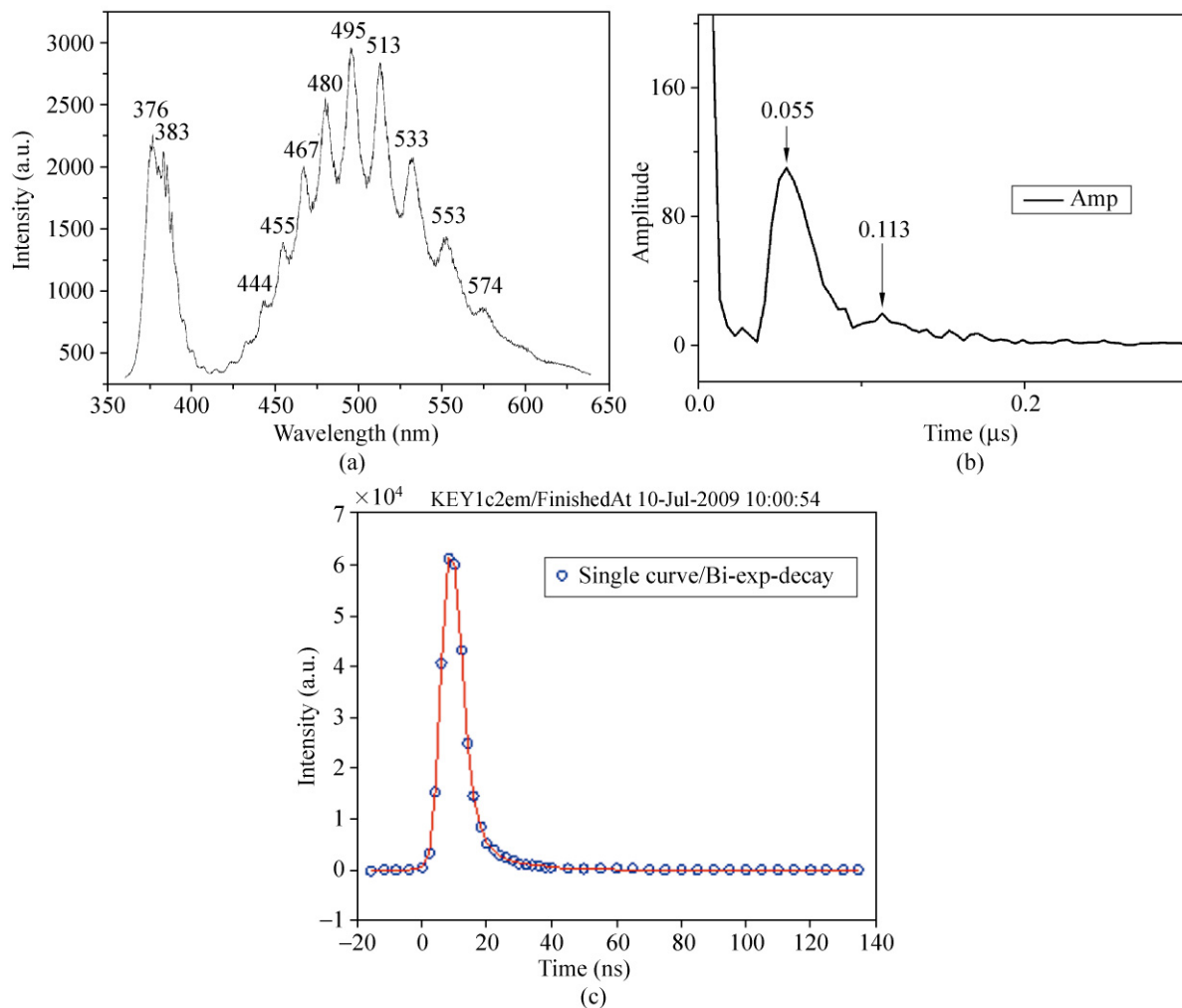


**Figure 8** (a) Room-temperature PL spectrum of the ZnO:ZnFe<sub>2</sub>O<sub>4</sub> 1-D PC when recording the Raman spectrum. (b) The Fourier transform of the visible range, indicating the lifetime profile of the optical cavity mode. (c) The decay line at 595 nm for this doped ZnO nanowire with excitation at 355 nm with a pulse width of 6.9 ns; this emission contains components with lifetime of 2.8 ns and 11.9 ns  $\pm$  4.0 ns

self-absorption. The emission mapping results are shown in Figs. 9(a)–9(k). Figure 9(a) is a PL mapping covering the whole wavelength range from 360 to 640 nm. The homogeneous intensity of the light along and across the MW indicates that there is no distinct difference in the luminescence after Fe(III) doping. A local PL mapping is made for each specific mode. For example, if we take the peak at 444 nm as the centre of the visible band, we scan over the wavelength range 441–447 nm. Figure 9(b) shows the mapping of UV emission, and no difference is detected. The mappings at wavelengths of 444, 455, 467, 480, 495, 513, 533, 553, and 574 nm are shown in Figs. 9(c)–9(k). As Fig. 9(c) shows, the mapping results exhibit a distinct periodic

distribution. It is noteworthy that the PL and Raman signals show almost the same periodic modulations, which provides indirect support for there being a local optical cavity effect in the wire.

The growth conditions can be adjusted to obtain different periodic wires. Figure 10(a) shows the PL spectrum of another MW with a larger periodic span. The insets on the left and right show the bright and dark images, respectively, in the CCD camera. The PL spectrum shows many more peaks than are observed in Fig. 8(b). The calculated cavity length using the formula in Ref. [45] is about 10  $\mu\text{m}$ , which is consistent with the mapping results for the Raman and PL spectra shown in Figs. 10(b) and 10(c).

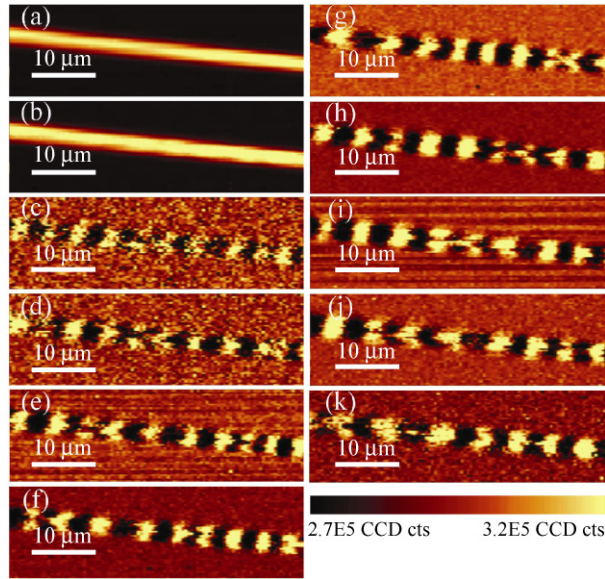


**Figure 9** Mapping images of the PL spectra: (a) the mapping collected from the whole wavelength range from 350 to 650 nm. (b)–(k) mapping images at wavelengths of 376, 444, 455, 467, 480, 495, 513, 533, 553, and 574 nm, respectively

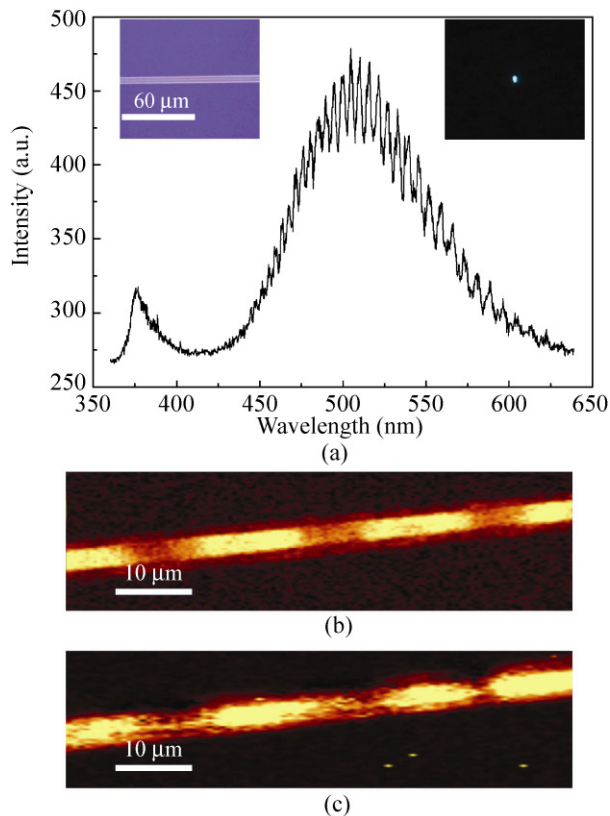


**Figure 10** (a) PL spectrum, (b) Raman mapping image, and (c) PL mapping image of another MW with larger periodic span than that used in obtaining the spectra and mappings shown in the earlier figures. The insets in (a) indicate the bright (left) and dark (right) field images in the CCD camera with the laser of 325 nm focused on the microwire

Since ZnO has a high dielectric constant and the MW itself is a very good waveguide, the photon inside the MW can be confined, and feedback between the two ends or different media of the MW act as a natural laser cavity. Many papers concerning lasing of ZnO have been reported. However, the reported lasing oscillation has always been in the UV region and has never been observed in the green range. The presence of appropriate conditions for cavity formation and the periodic peaks in the visible region can be attributed to spectral oscillation modes associated with Fe(III) doping in the MWs, and visible lasing lines may well be observed in other such structure in the future. The mappings show that the Fe has a periodic distribution in the ZnO MWs. The distance between every pair of highlights and dark regions is regular. The good agreement between the calculated and measured mapping lengths strongly indicates that the sharp lines are due to the longitudinal modes of a new optical cavity formed in the ZnO:ZnFe<sub>2</sub>O<sub>4</sub> MW.

How do these photons oscillate in an optical cavity in the MWs? Numerous different samples were investigated and we found that the PL mapping of some MWs showed a slightly irregular distribution of bright and dark regions rather than a perfect periodic variation. The refractive indices of ZnO and ZnFe<sub>2</sub>O<sub>4</sub> are 2.0 and 2.5, respectively [48], and their periodic distribution may be the origin of the multiple microcavities. After doping of Fe(III) into the MWs, the ZnFe<sub>2</sub>O<sub>4</sub> phase forms at periodic distances and ZnO:ZnFe<sub>2</sub>O<sub>4</sub> 1-D PCs result. When a laser is focused on this MW, a large number of photons are excited and propagate along the MW, with some being reflected and some passing through the ZnFe<sub>2</sub>O<sub>4</sub> layer or phase. The reflected photons meet another interface and are reflected again or pass through. Thus, cavity modes occur in the MW which depend on the local length of one cavity. In addition to the visible band, the UV emission shown in Fig. 8(a) also shows a multiplicity of bands, which is presumably also due to the optical cavity effect, which is more important for UV emission than the exciton splitting and phonon replication discussed above. Moreover, the optical cavity effect may be the dominant reason for the multiple peaks in the UV emission because of the short lifetime. If the

trapped states predominate in the MW, the lifetime may be much longer.

#### 4. Conclusions

We have synthesized ZnO:ZnFe<sub>2</sub>O<sub>4</sub> MW PCs by a simple controlled one-step thermal evaporation method. The MWs possess a novel rectangular cross section which is caused by the formation of a cubic ZnFe<sub>2</sub>O<sub>4</sub> phase on the ZnO MWs. The Raman spectra of the MWs show the typical Raman peaks of pure ZnO NWs and ZnFe<sub>2</sub>O<sub>4</sub>. Mappings of both individual Raman peaks and the whole spectra indicate a periodic modulation of the components along the MWs, as represented by their Raman distribution. The *in situ* PL spectra and *in situ* mapping also exhibit an oscillation, which indicates that there is a strong localization of photon propagation and oscillation along the longitudinal axis of the MWs. This behavior is typical of a coupled optical cavity in a wire. The physical origin of these phenomena is the difference in the refractive indices of the ZnO and ZnFe<sub>2</sub>O<sub>4</sub> components in the MW, whose periodic spatial distribution leads to the 1-D PC behavior.

This technique of producing F–P cavities along the MW may be applied to prepare other metal ion-doped ZnO MWs. These ZnO:ZnFe<sub>2</sub>O<sub>4</sub> MW PCs open a new era in the study of 1-D PCs in oxide semiconductors. These PCs have great potential for applications in lasing, waveguides, and light-slowing devices, as well as in solar cells and photon detectors. The Fe(III)-doped ZnO may also work as a 1-D spintronic material.

#### Acknowledgements

The authors thank the National Natural Science Foundation of China (NSFC) of China (Nos. 90606001, 20873039, and 90406024) for financial support.

**Open Access:** This article is distributed under the terms of the Creative Commons Attribution Noncommercial License which permits any noncommercial use, distribution, and reproduction in any medium, provided the original author(s) and source are credited.

#### References

- [1] Huang, M. H.; Mao, S.; Feick, H.; Yan, H. Q.; Wu, Y. Y.; Kind, H.; Weber, E.; Russo, R.; Yang, P. D. Room-temperature ultraviolet nanowire nanolasers. *Science* **2001**, *292*, 1897–1899.
- [2] Duan, X. F.; Huang, Y.; Agarwal, R.; Lieber, C. M. Single nanowire injection lasers. *Nature* **2003**, *421*, 241–245.
- [3] Cui, Y.; Wei, Q. Q.; Park, H. K.; Lieber, C. M. Nanowire nanosensors for highly sensitive and selective detection of biological and chemical species. *Science* **2001**, *293*, 1289–1292.
- [4] Barrelet, C. J.; Bao, J. M.; Lončar, M.; Park, H. G.; Capasso, F.; Lieber, C. M. Hybrid single-nanowire photonic crystal and microresonator structures. *Nano Lett.* **2006**, *6*, 11–15.
- [5] Agarwal, R.; Barrelet, C. J.; Lieber, C. M. Lasing in single cadmium sulfide nanowire optical cavities. *Nano Lett.* **2005**, *5*, 917–920.
- [6] Gradečak, S.; Qian, F.; Li, Y.; Park, H. G.; Lieber, C. M. GaN nanowire lasers with low lasing thresholds. *Appl. Phys. Lett.* **2005**, *87*, 173111.
- [7] Pan, A. L.; Liu, R. B.; Wang, F. F.; Xie, S. S.; Zou, B. S.; Zacharias, M.; Wang Z. L. High-quality alloyed CdS<sub>x</sub>Se<sub>1-x</sub> whiskers as waveguides with tunable stimulated emission. *J. Phys. Chem. B* **2006**, *110*, 22313–22317.
- [8] Schmidt-Mende, L.; MacManus-Driscoll, J. L. ZnO-nanostructures, defects, and devices. *Mater. Today* **2007**, *10*, 40–48.
- [9] Gorla, C. R.; Emanetoglu, N. W.; Liang, S.; Mayo, W. E.; Lu, Y.; Wraback, M.; Shen, H. Structural, optical, and surface acoustic wave properties of epitaxial ZnO films grown on (01-12) sapphire by metalorganic chemical vapor deposition. *J. Appl. Phys.* **1999**, *85*, 2595–2602.
- [10] Wang, X. D.; Zhou, J.; Song, J. H.; Liu, J.; Xu, N. S.; Wang, Z. L. Piezoelectric field effect transistor and nanoforce sensor based on a single ZnO nanowire. *Nano Lett.* **2006**, *6*, 2768–2772.
- [11] Jang, E. S.; Won, J. L.; Hwang, S. J.; Choy, J. H. Fine tuning of the face orientation activity. *Adv. Mater.* **2006**, *18*, 3309–3312.
- [12] Martin, P. M.; Good, M. S.; Johnston, J. W.; Posakony, G. J.; Bond, L. J.; Crawford, S. L. Piezoelectric films for 100-MHz ultrasonic transducers. *Thin Solid Films* **2000**, *379*, 253–258.
- [13] Chang, P. C.; Fan, Z. Y.; Chien, C. J.; Stichtenoth, D.; Ronning, C.; Lu, J. G. High-performance ZnO nanowire field effect transistors. *Appl. Phys. Lett.* **2006**, *89*, 133113.

- [14] Fan, Z. Y.; Lu, J. G. Zinc oxide nanostructures: Synthesis and properties. *J. Nanosci. Nanotechnol.* **2005**, *5*, 1561–1573.
- [15] Law, M.; Sirbully, D. J.; Johnson, J. C.; Goldberger, J.; Saykally, R. J.; Yang, P. D. Nanoribbon waveguides for subwavelength photonics integration. *Science* **2004**, *305*, 1269–1273.
- [16] Liu, C. H.; Zapien, J. A.; Yao, Y.; Meng, X. M.; Lee, C. S.; Fan, S. S.; Lifshitz, Y.; Lee, S. T. High-density, ordered ultraviolet light-emitting ZnO nanowire arrays. *Adv. Mater.* **2003**, *15*, 838–841.
- [17] Yuhas, B. D.; Zitoun, D. O.; Pauzauskie, P. J.; He, R. R.; Yang, P. D. Transition-metal doped zinc oxide nanowires. *Angew. Chem. Int. Ed.* **2006**, *45*, 420–423.
- [18] Liu, T.; Xu, H. R.; Chin, W. S.; Yang, P.; Yong, Z. H.; Wee, A. T. S. Local structures of  $Zn_{1-x}TM_xO$  (TM = Co, Mn, and Cu) nanoparticles studied by X-ray absorption fine structure Spectroscopy and multiple scattering calculations. *J. Phys. Chem. C* **2008**, *112*, 13410–13418.
- [19] Chu, D. W.; Zeng, Y. P.; Jiang, D. L. Synthesis of room-temperature ferromagnetic Co-doped ZnO nanocrystals under a high magnetic field. *J. Phys. Chem. C* **2007**, *111*, 5893–5897.
- [20] Yan, H. L.; Zhong, X. L.; Wang, J. B.; Huang, G. L.; Ding, S. L.; Zhou, G. C.; Zhou, Y. C. Cathodoluminescence and room temperature ferromagnetism of Mn-doped ZnO nanorod arrays grown by chemical vapor deposition. *Appl. Phys. Lett.* **2007**, *90*, 082503.
- [21] Barick, K. C.; Aslam, M.; Dravid, V. P.; Bahadur, D. Self-aggregation and assembly of size-tunable transition metal doped ZnO nanocrystals. *J. Phys. Chem. C* **2008**, *112*, 15163–15170.
- [22] Kundaliya, D. C.; Ogale, S. B.; Lofland, S. E.; Dhar, S.; Metting, C. J.; Shinde, S. R.; Ma, Z.; Varughese, B.; Ramanujachary, K. V.; Salamanca-Riba, L.; Venkatesan, T. On the origin of high-temperature ferromagnetism in the low-temperature-processed Mn–Zn–O system. *Nat. Mater.* **2004**, *3*, 709–714.
- [23] Jalbout, A. F.; Chen, H. N.; Whitternburg, S. L. Monte Carlo simulation on the indirect exchange interactions of Co-doped ZnO film. *Appl. Phys. Lett.* **2002**, *81*, 2217–2219.
- [24] Xu, C. X.; Sun, X. W.; Dong, Z. L.; Yu, M. B.; Xiong, Y. Z.; Chen, J. S. Magnetic nanobelts of iron-doped zinc oxide. *Appl. Phys. Lett.* **2005**, *86*, 173110.
- [25] Wang, Y. S.; Thomas, P. J.; O'Brien, P. Optical properties of ZnO nanocrystals doped with Cd, Mg, Mn, and Fe ions. *J. Phys. Chem. B* **2006**, *110*, 21412–21415.
- [26] Sato-Berrú, R. Y.; Vázquez-Olmos, A.; Fernández-Osorio, A. L.; Sotres-Martínez, S. Micro-Raman investigation of transition-metal-doped ZnO nanoparticles. *J. Raman Spectrosc.* **2007**, *38*, 1073–1076.
- [27] Baek, S. H.; Song, J. J.; Lim, S. W. Improvement of the optical properties of ZnO nanorods by Fe doping. *Physica B* **2007**, *399*, 101–104.
- [28] Bando, K.; Sawabe, T.; Asaka, K.; Masumoto, Y. Room-temperature excitonic lasing from ZnO single nanobelts. *Lumin J.* **2004**, *108*, 385–388.
- [29] van Vugt, L. K.; Rühle, S.; Vanmaeckelbergh, D. Phase-correlated nondirectional laser emission from the end facets of a ZnO nanowire. *Nano Lett.* **2006**, *6*, 2707–2711.
- [30] Yan, H. Q.; Johnson, J.; Law, M.; He, R. R.; Knutsen, K.; McKinney, J. R.; Pham, J.; Saykally, R.; Yang, P. D. ZnO nanoribbon microcavity lasers. *Adv. Mater.* **2003**, *15*, 1907–1911.
- [31] Czekalla, C.; Sturm, C.; Schmidt-Grund, R.; Cao, B. Q.; Lorenz, M.; Grundmann, M. Whispering gallery mode lasing in zinc oxide microwires. *Appl. Phys. Lett.* **2008**, *92*, 241102.
- [32] Johnson, J. C.; Choi, H. J.; Knutsen, K.; Schaller, R. D.; Yang, P. D.; Saykally, R. J. Single gallium nitride nanowire lasers. *Nat. Mater.* **2002**, *1*, 106–110.
- [33] Zhao, Y. H.; Abraham, M. H.; Zissimos, A. M. Determination of McGowan volumes for ions and correlation with van der Waals volumes. *J. Chem. Inf. Comput. Sci.* **2003**, *43*, 1848–1854.
- [34] Xiong, Q. H.; Chen, G.; Acord, J. D.; Liu, X.; Zengel, J. J.; Gutierrez, H. R.; Redwing, J. M.; Lew Yan Voon, L. C.; Lassen, B.; Eklund, P. C. Optical properties of rectangular cross-sectional ZnS nanowires. *Nano Lett.* **2004**, *4*, 1663–1668.
- [35] Zhang, D. F.; Sun, L. D.; Yin, J. L.; Yan, C. H.; Wang, R. M. Attachment-driven morphology evolution of rectangular ZnO nanowires. *J. Phys. Chem. B* **2005**, *109*, 8786–8790.
- [36] Robinson, R. D.; Sadtler, B.; Demchenko, D. O.; Erdonmez, C. K.; Wang, L. W.; Alivisatos, A. P. Spontaneous superlattice formation in nanorods through partial cation exchange. *Science* **2007**, *317*, 355–358.
- [37] Arguello, C. A.; Rousseau, D. L.; Porto, S. P. S. First-order Raman effect in wurtzite-type crystals. *Phys. Rev.* **1969**, *181*, 1351–1363.
- [38] Cuscó, R.; Alarcón-Lladó, E.; Ibáñez, J.; Artús, L. Jimenez, J.; Wang, B. G.; Callahan, M. J. Temperature dependence of Raman scattering in ZnO. *Phys. Rev. B* **2007**, *75*, 165202.
- [39] Gupta, V.; Blattacharya, P.; Yusuk, Y. I.; Sreenivas, K.;





- Katiyar, R. S. Optical phonon modes in ZnO nanorods on Si prepared by pulsed laser deposition. *J. Cryst. Growth*. **2006**, *287*, 39–43.
- [40] Wang, X. F.; Xu, J. B.; Zhang, B.; Yu, H. G.; Wang, J.; Zhang, X. X.; Yu, J. G.; Li, Q. Signature of intrinsic high-temperature ferromagnetism in cobalt-doped zinc oxide nanocrystals. *Adv. Mater.* **2006**, *18*, 2476–2480.
- [41] Wang, J. B.; Zhong, H. M.; Li, Z. F.; Lu, W. Raman study for  $E_2$  phonon of ZnO in  $Zn_{1-x}Mn_xO$  nanoparticles. *J. Appl. Phys.* **2005**, *97*, 086105.
- [42] Islam, E.; Sakai, A.; Onodera, A. Li-concentration dependence of micro-Raman spectra in ferroelectric-semiconductor  $Zn_1Li_{1-x}O$ . *J. Phys. Soc. Jpn.* **2002**, *71*, 1594–1597.
- [43] Liu, R. B.; Pan, A. L.; Fan, H. M.; Wang, F. F.; Shen, Z. X.; Yang, G. Z.; Xie, S. S.; Zou, B. S. Phonon-assisted stimulated emission in Mn-doped ZnO nanowires. *J. Phys. Condens. Matter* **2007**, *19*, 136206.
- [44] Wang, R. P.; Xu, G.; Jin, P. Size dependence of electron-phonon coupling in ZnO nanowires. *Phys. Rev. B* **2004**, *69*, 113303.
- [45] Zeng, H. B.; Cai, W. P.; Cao, B. Q.; Hu, J. L.; Li, Y.; Liu, P. S. Surface optical phonon Raman scattering in Zn/ZnO core-shell structured nanoparticles. *Appl. Phys. Lett.* **2006**, *88*, 181905.
- [46] Mohanta, A.; Thareja, R. K. Photoluminescence study of ZnO nanowires grown by thermal evaporation on pulsed laser deposited ZnO buffer layer. *J. Appl. Phys.* **2008**, *104*, 044906.
- [47] Fu, L. M.; Wu, Z. Y.; Ai, X. C.; Zhang, J. P.; Nie, Y. X.; Xie, S. S.; Yang, G. Z.; Zou, B. S. Time-resolved spectroscopic behavior of  $Fe_2O_3$  and  $ZnFe_2O_4$  nanocrystals. *J. Chem. Phys.* **2004**, *120*, 3406–3413.
- [48] <http://baike.baidu.com/view/1609325.html> (zinc ferrite pigment–refractive index)

